

Cite this article as: Xia Chaoqun, Li Ke, Cui Ziyao, et al. Corrosion Resistance Enhancement of Pure Zirconium in Various Environments via Microstructure Tailoring[J]. Rare Metal Materials and Engineering, 2024, 53(08): 2109-2122. DOI: 10.12442/j.issn.1002-185X.20230663.

ARTICLE

Corrosion Resistance Enhancement of Pure Zirconium in Various Environments via Microstructure Tailoring

Xia Chaoqun¹, Li Ke¹, Cui Ziyao², Song Tianshuo¹, Wu Xinyu¹, Liu Shuguang³, Zou Xianrui¹, Zhang Shiliang¹, Yang Tai¹, Li Qiang¹

¹Tianjin Key Laboratory of Materials Laminating Fabrication and Interface Control Technology, School of Materials Science and Engineering, Hebei University of Technology, Tianjin 300401, China; ²Industrial Technology Research Institute, Hebei University of Technology, Tianjin 300401, China; ³Engineering Research Center for Electrophysical Apparatus and Application Technology, Beijing Research Institute of Automation for Machinery Industry Co., Ltd, Beijing 100120, China

Abstract: The corrosion properties of pure zirconium (Zr) with different grain sizes in acid, alkali, and salt environments were studied. The microstructures of pure Zr were observed by optical microscope, X-ray diffractometer, and electron backscattered diffraction probe. The corrosion resistance of pure Zr was analyzed by electrochemical corrosion test and immersion test. Results show that pure Zr with grain size of 4–32 μm can be obtained after annealing at 800 °C for different durations, and the relationship between grain size and annealing duration is $D^3 - D_0^3 = 3.35t$. The electrochemical corrosion and immersion corrosion test results show that the pure Zr with grain size of about 24 μm (annealing at 800 °C for 20 h) possesses the optimal corrosion resistance.

Key words: pure zirconium; grain size; various environments; corrosion resistance

Zr is a very attractive metal in the nuclear industry due to its superior corrosion resistance, low thermal neutron absorption cross-sectional area, and good mechanical characteristics^[1]. Zr is also widely used in the chemical industry, particularly in the highly concentrated acidic and alkaline environments, and it is commonly used in chemical processes with exposure to strong acid bases^[2–3]. Moreover, Zr has been greatly applied in the preparation of implants and medical devices due to the emergence of biomedical materials with lower cytotoxicity, good biocompatibility, and outstanding corrosion resistance^[4–8]. However, the harsh application environment requires higher performance of Zr and its alloys. The material properties generally depend on the composition and processing methods. It is reported that the Hall-Patch formula explains the correlation between grain size and mechanical characteristics under specific conditions^[9]. Currently, the relationship between grain size and corrosion characteristics is still obscure.

With the emergence of ultrafine crystalline materials, more and more researches demonstrate that grain refinement can increase the corrosion resistance^[10–14]. Gu et al^[11] studied the corrosion behavior of pure titanium (Ti) in a 3.5wt% NaCl solution after equal-channel angular pressing (ECAP). It was found that the corrosion resistance of ultrafine crystalline pure Ti after ECAP is better than that of pure Ti with coarse crystalline structures. Attarilar et al^[12] reported that the grain refinement resulted in the rapid formation of strong oxidation bonds on the material surface, which improved the corrosion resistance of pure Ti. Braga et al^[13] showed that ECAP could affect the stress corrosion cracking susceptibility of aluminum alloys by affecting their grain size and local chemical properties. For the light metal Mg, the grain refinement can improve its corrosion resistance in neutral or alkaline sodium chloride solutions^[14] and the effect of grain size on corrosion resistance also depends on the combined effect of various factors, such as corrosive environment and process. Nie et

Received date: October 24, 2023

Foundation item: National Natural Science Foundation of China (52071126); Natural Science Foundation of Tianjin City, China (22JCQNJC01240); Central Guidance on Local Science and Technology Development Fund of Hebei Province (226Z1009G); Special Funds for Science and Technology Innovation in Hebei (2022X19); Foundation Strengthening Program (2019-JCJQ-00)

Corresponding author: Xia Chaoqun, Ph. D., Professor, Tianjin Key Laboratory of Materials Laminating Fabrication and Interface Control Technology, School of Materials Science and Engineering, Hebei University of Technology, Tianjin 300401, P. R. China, E-mail: chaoqunxia@hebut.edu.cn

Copyright © 2024, Northwest Institute for Nonferrous Metal Research. Published by Science Press. All rights reserved.

al^[15] investigated the corrosion resistance of pure Ti by high-pressure torsion (HPT) and reported that the pure Ti after annealing had better corrosion resistance in 3.5wt% NaCl solution than that after HPT processing. Annealing can reduce the residual stress after processing and regulate the grain size and texture distribution, which is an essential preparation process of Zr and Zr alloys^[16]. The effect of microstructure on the material properties is complex. Sahoo^[17] and Ghosh^[18] et al studied the evolution of weave texture of rolled pure Ti after annealing for different durations. Kim et al^[19] also reported that proper annealing treatment might enhance the corrosion resistance of pure Ti without strength degradation because of the change in the texture and dislocation density after annealing treatment.

Although the effect of microstructure on the corrosion behavior of pure Zr has been well researched, the relationship between grain size and corrosion resistance is rarely discussed. The primary purpose of this research is to investigate the impact of grain size on the corrosion resistance of pure Zr under different environments.

1 Experiment

The experiment material was a rolled pure Zr ($\geq 99.5\text{wt}\%$) plate with thickness of 3 mm. The heat treatment of pure Zr plates was conducted in a vacuum tube furnace under protective environment with high purity argon (99.999%). The heat treatment temperature was 800 °C and the treatment duration was 0 (namely the untreated state), 2, 6, 10, 20, and 40 h. The heating rate of the vacuum tube furnace was 5 °C/min. After heat treatment, the samples were cooled to room temperature in the furnace.

The sample microstructures were observed by optical microscope (OM, Axiom Vert A1). For OM observation, the samples were firstly cut into small pieces of 10 mm×10 mm×3 mm by EDM wire cutter, then ground, polished, and finally etched by the mixed solution of hydrofluoric acid, nitric acid, and deionized water with volume ratio of HF:HNO₃:H₂O as 1:3:5. X-ray diffractometer (XRD, Davinci D8 Focus) was used to assess the physical phase composition of the samples with copper target K α radiation and scanning range of 10°–90°. XRD samples were polished by 5000# silicon carbide sandpaper. The microstructures of the samples were further analyzed using electron backscattered diffractometer (EBSD, Oxford Symmetry), and the grain sizes and interfacial features of the samples were measured by AztecCrystal software. The grain size distribution data were fitted to lognormal and Gaussian distributions for analysis. The experiment voltage for EBSD test was 20 kV. EBSD test samples were ground, mechanically polished, and finally electrolytically polished. The electrolytic polishing solution was a mixed solution of 90vol% methanol and 10vol% perchloric acid, the operating voltage was about 20 V, and the operating current was about 2.6 A.

The electrochemical corrosion was measured by CHI660E electrochemical workstation equipped with three-electrode test equipment. The sample was served as the working

electrode, the auxiliary electrode was a platinum electrode, and the reference electrode was the saturated calomel electrode. The area of the platinum electrode in solution was 20 mm×20 mm. The electrolytes were 3.5wt% NaCl solution in order to simulate the natural seawater environment, 5wt% HCl solution, 0.1 mol/L NaOH solution to simulate the common industrial environment. The open circuit potential (E_{ocp}) tests were conducted for 1800 s, followed by the electrochemical impedance spectroscopy (EIS) tests in the frequency range of 10⁻²–10⁵ Hz. The potential amplitude for EIS testing was 5 mV, and at least 10 points were recorded between 0.1 and 0.01 Hz. Finally, the dynamic potential polarization tests were performed from -1200 mV to 2500 mV at the scanning rate of 10 mV/s. The samples were all cut into the blocks of 10 mm×10 mm×3 mm by EDM wire-cutting technique and then polished by 5000# SiC sandpaper. To further research the grain size effect on the corrosion characteristics of pure Zr, a white light interferometer (Leica, DCM8) was used to analyze the morphology of the samples after polarization in 5wt% HCl solution. Before tests, all samples were ultrasonically cleaned by deionized water and anhydrous ethanol for 20 min.

Immersion tests were conducted in the 5 mol/L HCl solution. The temperature of the immersion solution was room temperature (± 3 °C). The mass change and surface morphology of samples were used to assess corrosion properties. The cube immersion samples (10 mm×10 mm×3 mm) were prepared according to the following methods. Firstly, the observation side of EDM wire-cut sample was ground by 5000# silicon carbide sandpaper and the rest sides were ground by 1500# silicon carbide sandpaper. Secondly, the sample was ultrasonically cleaned with deionized water and anhydrous ethanol. During the immersion test (10 d), the samples were taken out every 2 d and cleaned ultrasonically with deionized water and anhydrous ethanol. Afterwards, the cleaned samples were weighed by electronic analytical balance. Finally, the samples were placed in a new immersion solution. Scanning electron microscope (SEM, JSM-7100F) was used to study the surface morphology of the immersed samples.

2 Results and Discussion

2.1 Phases

Fig. 1 shows XRD patterns of metallic Zr with different grain sizes. It can be seen that the variation in grain size barely has effect on the phase composition of Zr, the major crystalline facet of Zr is (0002), and the samples all have a densely arranged hexagonal structure of α -Zr. XRD peaks are shifted with the prolongation of annealing duration. As shown in Fig. 1b, the (10 $\bar{1}$ 1) crystal plane can be detected for the Zr in pristine state, but the intensity of the characteristic peaks is decreased with the prolongation of annealing duration. At the same time, the diffraction peaks become broadened. According to Bragg's Law, this phenomenon indicates that when the grain size of Zr changes, the orientation characteristics of the grains also change.

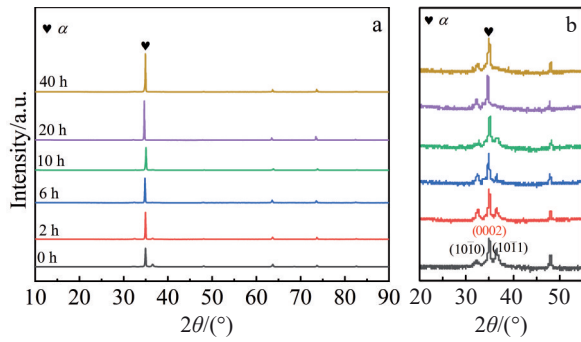


Fig.1 XRD patterns of pure Zr after annealing for different durations with $2\theta=10^{\circ}\text{--}90^{\circ}$ (a) and $2\theta=20^{\circ}\text{--}55^{\circ}$ (b)

2.2 Microstructures

OM morphologies of pure Zr after annealing at 800°C for different durations are shown in Fig.2. All samples have the equiaxed organization and the initial Zr grain size is around $4.7\ \mu\text{m}$. Changes in the annealing conditions cause changes in the grain size but do not induce phase transition. This is mainly because the annealing temperature is lower than the phase transition temperature. When the annealing duration is less than 10 h, the grain size and grain distribution of the sample change significantly. When the annealing duration is more than 10 h, the grain size of the sample increases, but the change is not noticeable. At the same time, the grain

distribution of pure Zr tends to be homogeneous, and the small grains gradually grow into large grains. According to Fig.2f, the grain size of the sample after annealing for 40 h is approximately $40\ \mu\text{m}$, because the prolonged high-temperature heat treatment accelerates the grain growth^[20].

Fig. 3 shows the inverse pole figures (IPFs) of grain orientations of pure Zr after annealing at 800°C for different durations, and the corresponding antipodal coordinate system is shown in the inset of Fig. 3a. Combining the grain orientation distribution and the antipodal coordinate system, it can be concluded that the grain sizes of the samples are significantly different. The initial samples are mainly composed of small grains. With the prolongation of annealing duration, the grain size of the samples is increased gradually. According to Fig.3f, the sample is mainly composed of large grains. Meanwhile, the initial grain orientation of the sample is mainly (0001), followed by (01 $\bar{1}$ 0) orientation. With the increase in grain size, the grain orientation becomes closer to (0001), which indicates that the grain size and crystal orientation change simultaneously.

Fig.4 and Fig.5 show the antipodal and polar figures (PFs) of pure Zr after annealing for different durations, respectively. Based on IPFs and PFs of EBSD analysis, it is possible to qualitatively analyze the texture and phase composition in the material. Combining PFs and antipodal plots, it is found that all pure Zr samples exhibit a clear (0001)//normal direction

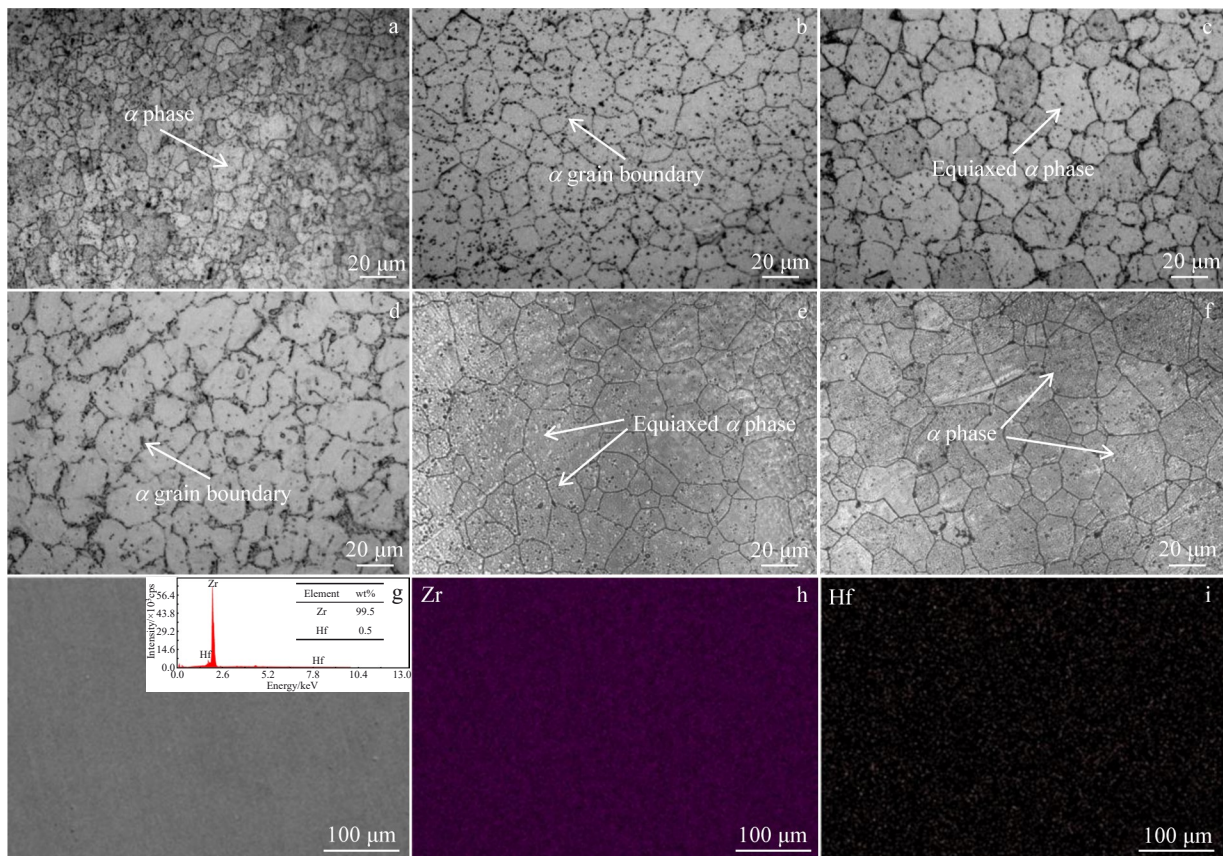


Fig.2 OM morphologies of pure Zr after annealing at 800°C for 0 h (a), 2 h (b), 6 h (c), 10 h (d), 20 h (e), and 40 h (f); EDS analysis results of untreated pure Zr (g); EDS element distributions of Zr (h) and Hf (i) in untreated pure Zr

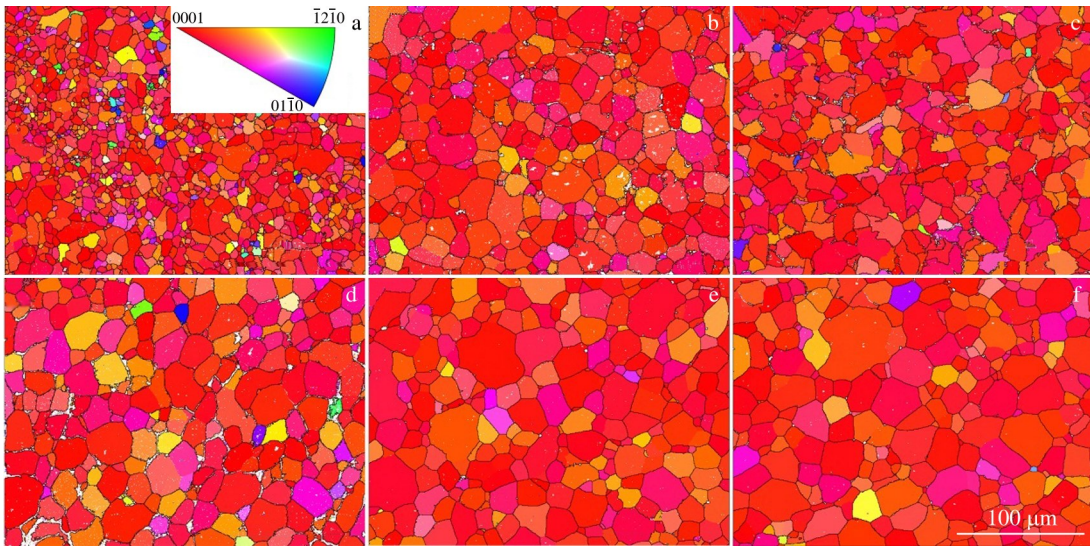


Fig.3 IPFs of grain orientations in pure Zr after annealing at 800 °C for 0 h (a), 2 h (b), 6 h (c), 10 h (d), 20 h (e), and 40 h (f)

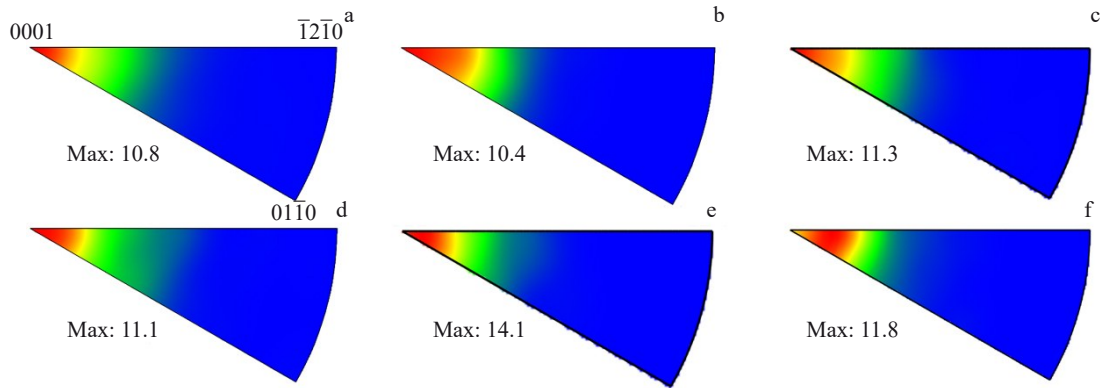


Fig.4 Antipodal plots for EBSD analysis of pure Zr after annealing at 800 °C for 0 h (a), 2 h (b), 6 h (c), 10 h (d), 20 h (e), and 40 h (f)

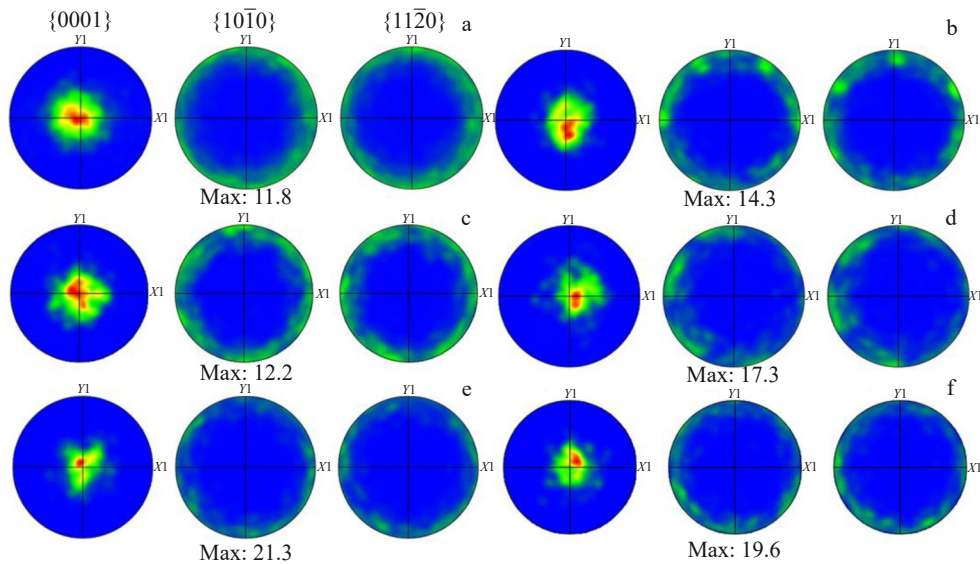


Fig.5 PFs for EBSD analysis of pure Zr after annealing at 800 °C for 0 h (a), 2 h (b), 6 h (c), 10 h (d), 20 h (e), and 40 h (f)

texture. With the change in grain size, i. e., the annealing duration, the weave strength is changed. The weave strength of pure Zr after annealing for 20 h reaches about 21, which is

higher than that of other samples. Fig.6 shows the grain size distributions of pure Zr after annealing for different durations. The grain size distribution of the coarse crystals is broader

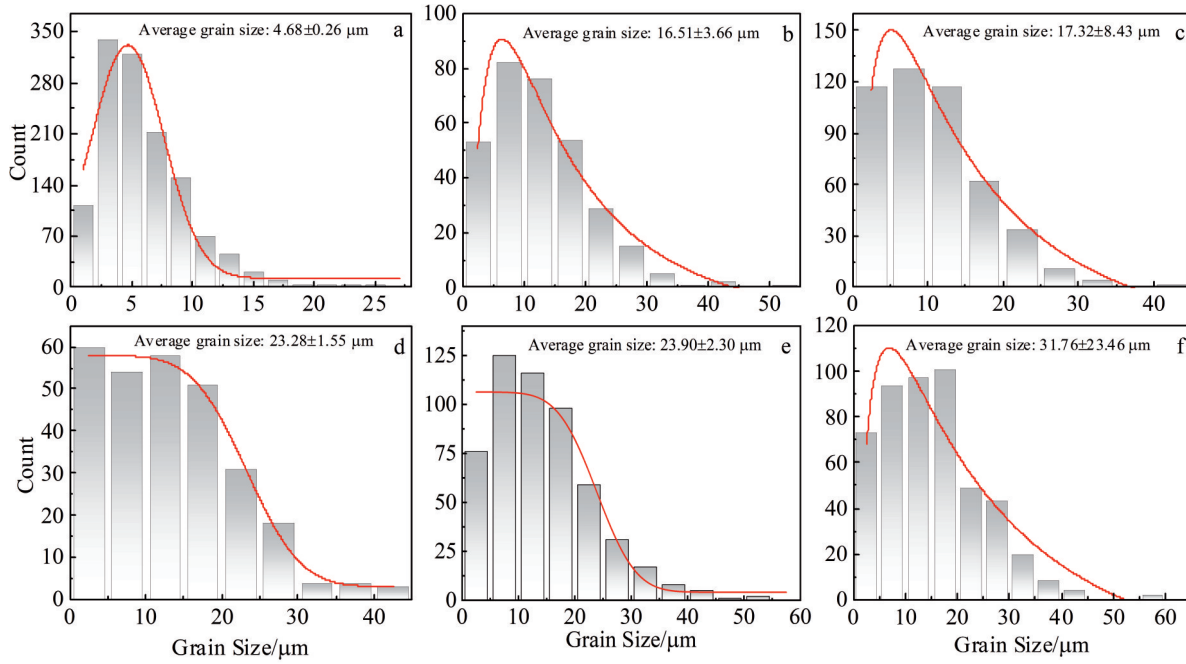


Fig.6 Grain size distributions of pure Zr after annealing at 800 °C for 0 h (a), 2 h (b), 6 h (c), 10 h (d), 20 h (e), and 40 h (f)

than that of other samples, and this phenomenon may be related to the inhomogeneity of annealing. The grain size of the untreated sample is mainly 0–10 μm with an average grain size of about 4 μm. As shown in Fig.6f, the range of grain size of the coarse crystals is 4–60 μm, and therefore the average grain size of the coarse crystal sample is about 32 μm. The grain size of other samples mainly ranges from 10 μm to 25 μm. The average grain size of the sample after annealing for 20 h is approximately 24 μm. In addition, Table 1 shows the proportion of grain boundary orientations, such as high-angle grain boundaries (HAGBs) and low-angle grain boundaries (LAGBs). It can be seen that the grain boundary orientations are changed with the grain size. The untreated sample has the highest percentage of HAGBs and the sample after annealing for 10 h has the lowest percentage of HAGBs. The effect of annealing on grain boundary orientation is also reflected by the annealing of CrCoNi medium entropy alloys^[21].

2.3 Dynamic analysis of grain growth

Fig. 7a shows the grain size of annealed samples as a function of annealing duration. It can be seen that with the prolongation of annealing duration, the grain size is increased, but the growth rate of the grains is decreased during isothermal annealing, which is consistent with the growth patterns in most metallic materials. According to Fig. 7a, the relationship of $\ln(dD/dt) - \ln D$ can be obtained, as shown in Fig. 7b. Thus, the grain growth rate can be obtained by Eq.(1)^[22], as follows:

$$\ln(dD/dt) = \ln(k/n) - (n - 1)\ln D \quad (1)$$

where D is the average grain size of samples after annealing at 800 °C for different durations; t is annealing duration; n and k are constants. According to the linear fitting analysis of Fig. 7b, the n value is taken as an integer of 3 and the k value is 3.35. Therefore, by integrating Eq. (1), the relationship between grain size and annealing duration can be obtained, as follows:

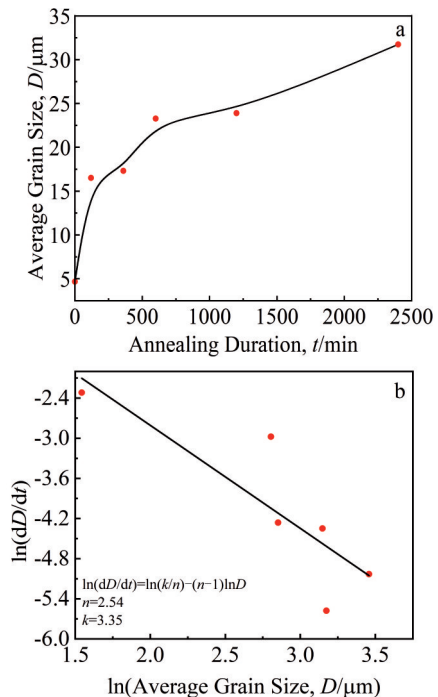


Fig.7 Relationship of average grain size with annealing duration (a) and $\ln(dD/dt) - \ln D$ (b)

Table 1 Grain boundary orientation distributions of pure Zr after annealing for different durations

Duration/h	0	2	6	10	20	40
HAGB/%	94.1	91.5	91.1	90.3	93.4	93.6
LAGB/%	5.94	8.54	8.87	9.72	6.58	6.37

$$D^3 - D_0^3 = 3.35t \quad (2)$$

where D_0 is the grain size of untreated Zr.

2.4 Electrochemical corrosion test

The electrochemical corrosion characteristics of samples with different grain sizes were investigated through the tests in 5wt% HCl, 0.1 mol/L NaOH, and 3.5wt% NaCl solutions. Firstly, open circuit potential (OCP) test was performed on the sample with the typical three-electrode system.

Fig. 8a demonstrates the variation of OCP with time in 5wt% HCl solution. In the first 800 s, OCP value moves to a low level and the curve is chaotic, which indicates that the surface state of the samples is unstable and the production and dissolution of passivation films cannot reach a dynamic equilibrium. After 800 s, OCP moves in the positive direction and it is higher than the initial potential. Sustained stabilization is attained after 1600 s, and the potential finally stabilizes between -0.4 and 0.2 V. This result suggests that the tested samples not only generate a protective film, but also

attain a dynamic equilibrium between the formation and dissolution of the oxide film on the pure Zr surface^[23]. Fig. 8b shows typical kinetic potential polarization curves for samples tested in 5wt% HCl solution. Table 2 presents the polarization data obtained by linear extrapolation. With the increase in the extrapolation potential from -1.2 V to the corrosion potential E_{corr} , the current density is decreased for all samples, and all tested materials have similar cathodic branches with cathodic slopes in the similar ranges, which suggests that cathodic reactions occurring on the surfaces of all samples are similar^[24]. Regarding the anodic branch, the anodic polarization curve contains more regions. Firstly, the current density of the tested samples rises sharply from the corrosion potential point with the increase in applied potential, which results from the activated polarization, indicating that the passivation film is generated at this stage^[25]. From -0.3 V to pitting potential, the current density presents an insignificant upward trend with the increase in potential, and the stable current density at this time is regarded as the dimensional

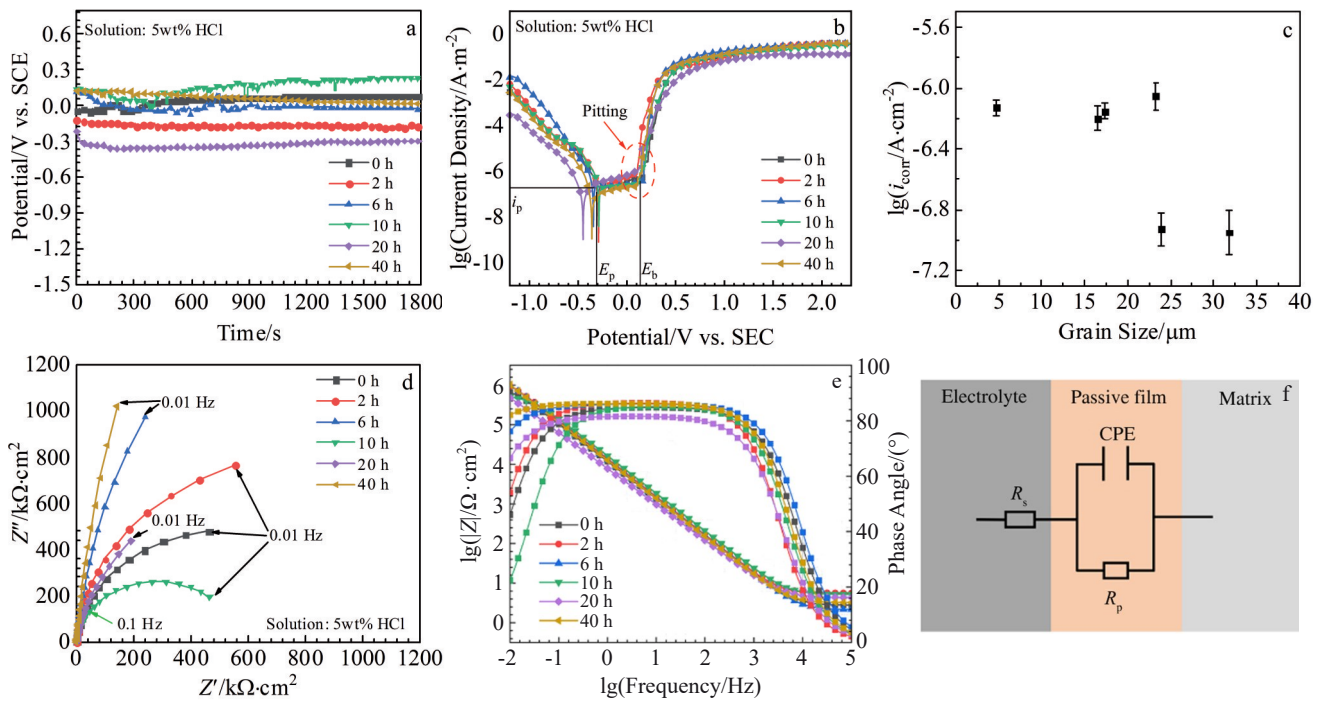


Fig.8 Electrochemical test results of pure Zr after annealing at $800\text{ }^{\circ}\text{C}$ for different durations in 5wt% HCl solution: (a) OCP curves; (b) potential polarization curves; (c) relationships between corrosion current density and grain size; (d) Nyquist plots; (e) Bode impedance plots; (f) schematic diagram of equivalent circuit model

Table 2 Kinetic potential polarization parameters of pure Zr after annealing at $800\text{ }^{\circ}\text{C}$ for different durations in 5wt% HCl, 0.1 mol/L NaOH, and 3.5wt% NaCl solutions

Parameter	Solution	0 h	2 h	6 h	10 h	20 h	40 h
Corrosion potential, $E_{\text{corr}}/\text{mV}$	3.5wt% NaCl	-636 ± 08	-484 ± 32	-406 ± 15	-683 ± 31	-675 ± 24	-787 ± 46
	0.1 mol/L NaOH	-527 ± 26	-217 ± 06	-360 ± 35	-622 ± 11	-567 ± 15	-588 ± 31
	5wt% HCl	-293 ± 23	-290 ± 63	-343 ± 21	-287 ± 49	-449 ± 43	-359 ± 09
Corrosion current density, $i_{\text{corr}}/\times 10^{-7}\text{ A}\cdot\text{cm}^{-2}$	3.5wt% NaCl	0.33 ± 0.07	0.46 ± 0.07	0.62 ± 0.25	0.29 ± 0.10	0.23 ± 0.43	0.87 ± 0.39
	0.1 mol/L NaOH	0.57 ± 0.17	16.14 ± 6.37	2.24 ± 1.13	0.32 ± 0.43	0.23 ± 1.97	0.32 ± 0.13
	5wt% HCl	7.43 ± 3.21	6.32 ± 3.10	7.04 ± 3.66	8.84 ± 3.69	1.17 ± 0.98	1.12 ± 3.23

passivation current density (i_p), which suggests that a protective passivation film is formed on the sample surface to prevent further corrosion^[26]. Additionally, at this stage, the current density is closely related to the finite rate of passivation film evaporation^[27]. Regarding the formation process and the nature of the passivation film, the phase-forming film theory and the adsorption theory have different explanations, but both theories indicate that the passivation film generated at this time on the sample surface shows protective effect and can reduce the corrosion rate of the metals^[28-29]. Then, the lengths between the corrosion potential and the pitting potential are not the same, and the sample annealed for 20 h has the widest range of passivation platforms, indicating that its comprehensive resistance against pitting corrosion is better. After the applied potential exceeds 0.2 V, the current density rises sharply with the increase in applied potential, which is the result of the dissolution and breakdown of the surface protection film. In addition, the passivation layer generated on the sample surface becomes unstable at higher anodic potentials, which leads to the decreased protective effect of the passivation film, according to the quickly rising current density. Some pits exist on the macro surface. The corrosion potential indicates the corrosion tendency of the material, and the corrosion current density i_{corr} suggests the corrosion rate. The corrosion potentials of all samples are between -0.4 and -0.3 V. The most negative self-corrosion potential is obtained for the sample annealed for 20 h, which indicates that the corrosion tendency of the sample is the highest. The corrosion current density of pure Zr with different grain sizes, namely after annealing at 800 °C for different durations, is provided in Fig. 8c, and it is clear that the corrosion current density shows a decreasing tendency, then increases, and finally decreases with the grain growth. The sample annealed for 10 h has the largest corrosion current density (8.84×10^{-7} A/cm²) and the worst corrosion resistance. Since the corrosion current densities of pure Zr annealed for 20 and 40 h are close to each other, the passivated film resistance (R_p) obtained from the impedance results and the polarization results is related to the corrosion resistance, and their order is as follows: 20 h > 40 h > 2 h > 6 h > 0 h > 10 h.

Electrochemical impedance test was conducted to discuss the properties of passivation film on the metal surface and the electrochemical characteristics of the system. Fig. 8d–8e show the impedance diagram results of the samples in 5wt% HCl solution. The impedance plots show that all samples exhibit a single time constant electrochemical impedance response in 5wt% HCl solution, which suggests that the electrochemical corrosion procedure is charge-transfer controlled^[30]. In Fig. 8d, the Nyquist plots of all samples show a single capacitive arc, and the capacitive arc radius represents the level of resistance of the sample surface passivation film. The larger the radius, the better the corrosion resistance. Fig. 8e shows the Bode plots of all samples in 5wt% HCl solution. The Bode impedance plots of all samples display two phases. In the high-frequency region, the impedance plots show a segment with the slope close to 0. This indicates that the impedance in the

high-frequency region represents the resistance of the electrolyte solution, and this phenomenon is represented by the phase angle close to 0°. In the mid-frequency and low-frequency regions, the impedance plots are mainly straight with a slope of -1, which suggests that the frequency range correlates with the capacitive response of the passivated layer. In the solutions containing chloride ions, Zr and Zr alloys are more susceptible to chloride ion attack and pitting corrosion. Meanwhile, according to the pitting defect model, it is known that in the solution containing chloride ions, Cl⁻ is more likely to occupy the oxygen vacancy from the solution, form cationic vacancies at the oxide/electrolyte interface, and undergo diffusion and annihilation, thus forming localized corrosion and pitting corrosion^[31].

Since Nyquist plot shows a single time constant capacitive resistance arc and the curve deviates slightly from a semicircle, a constant phase angle element (CPE) is used instead of the ideal capacitor and it is fitted using the equivalent circuit model, as shown in Fig. 8f. R_s is the solution resistance, R_p is the passivated film resistance, and R_p is parallel to CPE. The impedance value of CPE (Z_{CPE}) can be defined as follows:

$$Z_{CPE} = Y_0^{-1} (j\omega)^{-n} \quad (3)$$

where Y_0 represents the true capacitance of CPE in Sⁿ/Ω; j is an imaginary number; ω is the angular frequency; n ($-1 \leq n \leq 1$) is the dispersion index of CPE, indicating the degree of deviation from the ideal capacitance. The n value is related to the stability of the passivation layer and the inhomogeneous currents caused by the presence of defects. The closer the n value to 1, the more dense the passivation film, and the smaller the surface roughness of the oxide film^[32]. In addition, since CPE is commonly used to de-characterize the frequency dependence under non-ideal capacitance, the effective capacitance value (C_{eff}) of the passivation film can be deduced from the unit of Y_0 value with the unit of capacitance C as S/Ω or F, as follows^[33]:

$$C_{eff} = Y_0 (f_m)^{n-1} \quad (4)$$

where f_m denotes the frequency at which the imaginary portion of the impedance plot reaches the highest value. EIS data fitted by the equivalent circuit diagram with the effective capacitance value (C_{eff}) are presented in Table 3. According to Table 3, the solution resistance (R_s) values of all samples in the same solution are similar. Ref. [34–36] show that the smaller the values of effective capacitance (C_{eff}) and Y_0 , the higher the values of n and passivation film resistance (R_p), the better the passivation film performance of the sample, and the better the corrosion resistance. Therefore, according to the data in Table 3, it can be concluded that in 5wt% HCl solution, the coarse crystalline samples annealed for 20 h have higher R_p values and better corrosion resistance compared with the fine crystalline samples without annealing. The relationship between grain size and corrosion resistance in a certain range is complex and non-monotonic. In addition, since the electrochemical impedance test is more susceptible to external interference, the electrochemical impedance data are only used as a reference result for the electrochemical

Table 3 Fitted EIS analysis results of pure Zr after annealing at 800 °C for different durations in 5wt% HCl, 0.1 mol/L NaOH, and 3.5wt% NaCl solutions

Solution	Annealing duration/h	$R_s/\Omega\cdot\text{cm}^2$	$Y_0/\times 10^{-5} \text{ S}^n\cdot\Omega\cdot\text{cm}^{-2}$	$C_{\text{eff}}/\times 10^{-5} \text{ F}\cdot\text{cm}^{-2}$	n	$R_p/M\Omega\cdot\text{cm}^2$	$\chi^2/\times 10^{-3}$
3.5wt% NaCl	0	14.64±0.37	1.12±0.17	1.44±0.33	0.95±0.01	39.58±1.29	0.77±1.50
	2	15.75±4.30	1.27±0.10	1.57±0.17	0.95±0.01	4.65±2.19	2.57±0.76
	6	15.91±0.80	1.86±0.29	2.87±0.64	0.91±0.03	6.77±1.59	8.22±3.49
	10	15.60±1.25	1.37±0.16	1.66±0.17	0.96±0.03	12.31±5.08	1.91±0.77
	20	15.88±1.08	1.03±0.70	1.41±1.74	0.93±0.05	13.3±6.46	1.44±3.27
	40	16.07±1.17	1.25±0.05	1.74±0.08	0.93±0.01	6.69±3.39	1.16±0.52
	0	2.75±0.82	1.48±4.13	1.91±0.78	0.94±0.06	1.05±0.97	2.45±0.32
5wt% HCl	2	5.59±2.83	1.23±0.78	1.47±0.80	0.96±0.30	1.75±3.30	1.50±0.14
	6	2.13±1.75	1.37±1.04	1.67±1.51	0.96±0.18	5.84±0.33	1.18±0.04
	10	5.13±1.87	1.06±1.29	1.33±3.77	0.95±0.03	0.56±0.32	3.87±1.39
	20	4.28±1.09	2.41±0.44	3.66±0.79	0.91±0.04	1.80±3.19	4.07±1.53
	40	3.23±1.77	1.37±0.54	1.66±1.76	0.96±0.06	1.41±0.29	3.34±0.35
0.1 mol/L NaOH	0	44.77±3.77	1.17±0.41	1.61±1.20	0.93±0.04	0.67±1.17	3.48±0.02
	2	51.76±7.21	1.69±0.25	2.57±0.24	0.91±0.02	0.01±0.002	8.89±2.67
	6	40.12±6.23	1.16±0.23	1.40±0.55	0.96±0.03	3.29±0.10	3.09±1.53
	10	41.04±3.12	0.95±0.84	1.26±3.15	0.94±0.08	1.03±1.27	2.59±0.01
	20	45.63±3.28	0.95±0.63	1.20±2.18	0.95±0.08	5.71±2.43	3.57±0.01
40	57.06±5.66	1.18±0.07	1.91±0.24	0.90±0.02	5.44±0.94	4.40±0.61	

corrosion tests of samples. Eq. (5)^[30] shows the relationship between C_{eff} value and the thickness of oxide film d , as follows:

$$d = \varepsilon \varepsilon_0 A / C_{\text{eff}} \quad (5)$$

where ε and ε_0 represent the dielectric constant of the oxide film and the vacuum dielectric constant, respectively; A is the area of 1 cm². The film thickness can be obtained by calculation and its results are recorded in Table 4. It can be seen that the pure Zr with the grain size of approximately 24 μm (annealing for 20 h) has the highest degree of orientation strength and forms the thickest oxide film, and the enhanced passivation film thickness correlates to the improved corrosion resistance. The value of ε (ZrO₂) is 26 F/cm and ε_0 is 8.854×10⁻¹⁴ F/cm. The value of χ^2 is used to verify the proximity between the electrochemical impedance results fitted by the adopted equivalent circuit model and the measured experiment data. It can be seen from Table 3 that the values of χ^2 for all samples are in the order of 10⁻³, indicating that this equivalent circuit model can fit the measured experimental data. In conclusion, EIS analysis results are consistent with the kinetic potential polarization results.

Fig. 9a demonstrates OCP results in 3.5wt% NaCl solution. With the increase in the grain size, OCP curves of all samples

show similar variation trends: the potentials slightly decrease or remain stable. The final steady point is between -0.18 and -0.42 V, which indicates that the thin films on the sample surface have already been damaged by dissolution in the early test stage, so their densification and protection effects are reduced^[37]. For the samples annealed at 800 °C for 2 h, the curve changes abruptly around 1300 s, which may be due to system instability or external interference. Fig. 9b shows the typical kinetic potential polarization curve of the metals in 3.5wt% NaCl solution. For the coarse crystalline sample (annealing for 40 h), the applied potential varies from -0.67 V to -0.2 V. The current density remains constant with the increase in applied potential, and this region is known as the passivation zone, inferring that a protective passivation film is generated on the sample surface to prevent further corrosion^[36]. When the applied potential reaches about 0 V, the current density of the sample increases in proportion to potential, indicating that at this time, the passivation film on the sample surface is destroyed and pitting corrosion occurs. When the applied potential reaches about 0.6 V, the current density remains stable and a small platform can be observed. When the potential reaches about 1.61 V, the current density increases sharply. This phenomenon proves that the passiva-

Table 4 Film thickness d of pure Zr after annealing at 800 °C for different durations in 5wt% HCl, 0.1 mol/L NaOH, and 3.5wt% NaCl solutions

Solution	0 h	2 h	6 h	10 h	20 h	40 h
3.5wt% NaCl	1.599	1.466	0.802	1.387	1.633	1.323
5wt% HCl	1.205	1.566	1.378	1.730	0.629	1.387
0.1 mol/L NaOH	1.430	0.896	1.644	1.827	1.918	1.205

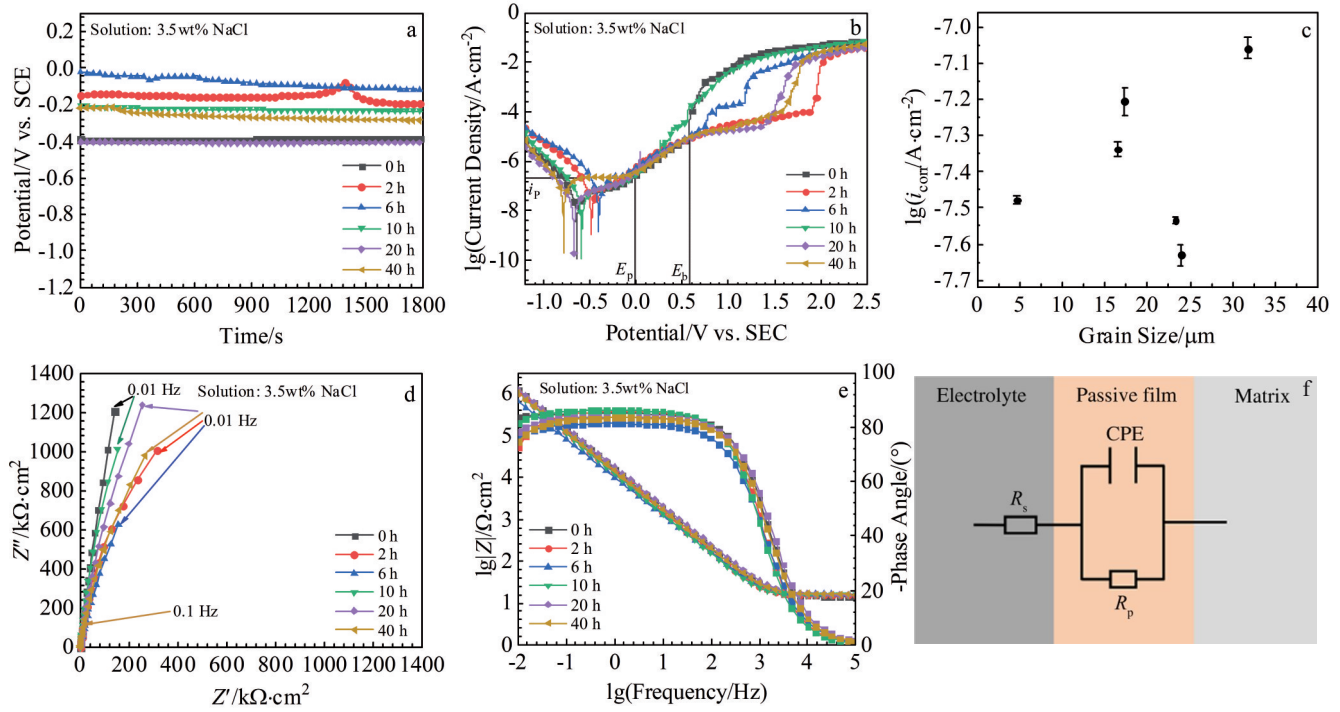


Fig.9 Electrochemical test results of pure Zr after annealing at 800 °C for different durations in 3.5wt% NaCl solution: (a) OCP curves; (b) potential polarization curves; (c) relationships between corrosion current density and grain size; (d) Nyquist plots; (e) Bode impedance plots; (f) schematic diagram of equivalent circuit model

tion film of the coarse crystalline samples is destroyed and then regenerated, so the sample suffers dissolution and pitting corrosion before the film regeneration. This is mainly because Ti and Zr metals have a certain degree of self-healing ability, and the surface passivation film can be regenerated^[38]. Fig.9b shows that the secondary pitting phenomenon does not occur in all samples, which indicates that the samples with different grain sizes have different Cl⁻ pitting resistance. In addition, the fragile passivation film generated on the metal surface can be inferred by the quickly rising current density, and the pitting occurs at higher anodic potentials when the protective effect of the passivation film is weakened. The fact that the high sensitivity of Zr and Zr alloys to chloride ion pitting is not negligible is the side evidence^[39]. The values of E_{corr} and i_{corr} are determined by the kinetic potential curve using the Tafel extrapolation method, and the results are shown in Table 2. As shown in Fig. 9c, the corrosion current density of the samples is firstly increased and then decreased with the increase in grain size. Besides, the corrosion resistance of sample annealed for 20 h is optimal, and the worst corrosion resistance is obtained for the coarse crystalline sample after annealing for 40 h, which suggests that the increase in grain size within a certain range can improve the corrosion resistance. According to Table 2, it is evident that the order of corrosion current density of pure Zr from small to large (corrosion resistance from strong to weak) is 20 h < 10 h < 0 h < 2 h < 6 h < 40 h. The reasons for this phenomenon are described as follows.

On the one hand, as shown in Fig.2 and Fig.6, the samples

after annealing for a long time have a more uniform grain distribution and a more concentrated grain size distribution. Ref. [40] reported that corrosion resistance is determined by the microstructural characteristics, including grain size, grain boundary distribution, and the proportion of HAGBs. Under certain conditions, increasing grain boundary length leads to the increase in corrosion potentials and pitting potentials as well as the reduction in corrosion current density.

On the other hand, during the annealing process, the change in grain size is accompanied by the change in grain orientation. According to Ref. [41], the effect of crystal orientation on corrosion may be greater than that of grain size under certain conditions. It can also be seen from Fig.1 and Fig.4 that the grain orientation of the material changes subtly with the change in grain size.

Fig. 9d – 9e demonstrate the electrochemical impedance results for the samples tested in 3.5wt% NaCl solution. All Nyquist plots (Fig.9d) show semicircular arcs similar to those in HCl solution, which are associated with the development of a surface-based complete passive barrier film. The equivalent circuit model employed in test with 5wt% HCl is also applicable to the situation with 3.5wt% NaCl solution. The results fitted through the model are summarized in Table 3. In 3.5wt% NaCl solution, the fine grain sample (without annealing) has the highest R_p value, which corresponds to the optimal corrosion resistance, and the coarse grain Zr sample with grain size of about 30 μm (annealing for 20 h) has the second highest corrosion resistance. The magnitude of the R_p value represents the dissolution response rate of samples and

the resistance against the charge transmission through the film. The χ^2 values for all samples are in the order of 10^{-3} , which indicates that the fitting results with this equivalent circuit model are reasonable.

Fig. 10a demonstrates OCP results of samples in 0.1 mol/L NaOH solution. The positive shift of OCP for most samples indicates the formation of a protective passivation film on the sample surface^[21], and the final potential is stable between -0.2 and -0.6 V. Fig. 10b shows the typical kinetic potential polarization curves of samples tested in 0.1 mol/L NaOH solution. All samples exhibit similar cathodic curves, indicating that similar cathode reactions occur on the sample surfaces. In the anodic curve stage, except that of the sample annealed for 10 h, the activation-passivation transition zones of the rest samples are not obvious, suggesting the polarization curves without an obvious passivation zone, and the corrosion current density increases rapidly when the potential reaches about 0 V. The main reason is that the cathodic reaction potential is higher than the passivation

potential, and the intersection point of the cathodic and anodic curves is in the passivation area, which indicates that the self-passivated metal forms a protective film with the lower corrosion potential on the surface. This film is more stable and less likely to be destroyed in the sodium hydroxide solution. Through macroscopic observation of the sample surface after polarization, it is found that there are no obvious pitting pits on the sample surface. Table 2 shows the polarization data obtained by linear extrapolation. The corrosion potential is the greatest for the sample annealed for 2 h, which indicates that corrosion tends to occur less frequently at this grain size. The corrosion thermodynamics can be described by the corrosion potentials, and the corrosion current density is the most important parameter to account for the corrosion kinetics. Fig. 10c shows that the sample annealed for 2 h has the highest corrosion current density, indicating the worst corrosion resistance. Based on the data in Table 2, the corrosion resistance from the strongest to the weakest can be arranged in order as 20 h>40 h (coarse grain)>10 h>0 h (fine grain)>6 h>

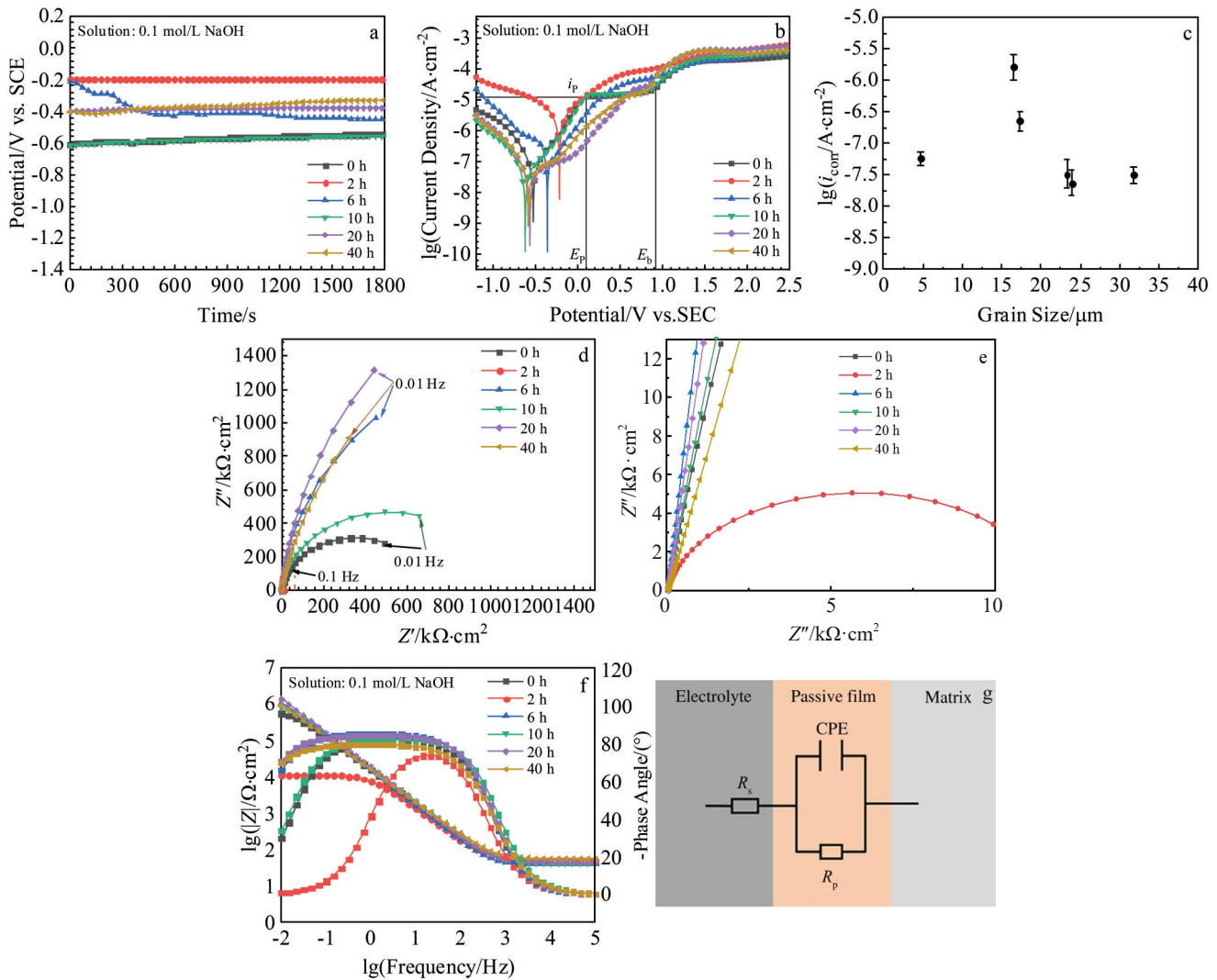


Fig.10 Electrochemical test results of pure Zr after annealing at 800 °C for different durations in 0.1 mol/L NaOH solution: (a) OCP curves; (b) potential polarization curves; (c) relationships between corrosion current density and grain size; (d–e) Nyquist plots; (f) Bode impedance plots; (g) schematic diagram of equivalent circuit model

2 h. Comparing the polarization results of Zr metal in NaCl, HCl, and NaOH solutions, it can be found that the Zr sample presents better corrosion resistance in alkaline solution. The passivation film of the sample in alkaline solution is very stable and barely has damage to the sample surface, and Zr metal can remain passivated for a longer time with very low corrosion rate.

Fig. 10d–10e show EIS results of the samples tested in 0.1 mol/L NaOH solution. All samples show the electrochemical impedance response with a single time constant, which suggests that the electrochemical corrosion procedure is charge-transfer controlled^[30]. The Nyquist plots (Fig. 10d) show that the sample annealed for 20 h has the optimal corrosion resistance, whereas the sample annealed for 2 h has the worst corrosion resistance. The equivalent circuit model used in the tests with 5wt% HCl solution is also applied to the tests with 0.1 mol/L NaOH solution. In the 0.1 mol/L NaOH solution, the coarse crystalline pure Zr (annealing for 20 h) has the lowest effective capacitance (C_{eff}), its n value is close to 1, and its solution resistance R_p is the largest, which indicates that this sample produces a denser and more stable passivation film in the electrolyte, exhibiting better corrosion

resistance. The χ^2 values of all samples are in the order of 10^{-3} , which indicates that the equivalent circuit model is reasonable to fit the measured experiment data.

2.5 Immersion test analysis

Fig. 11a–11f illustrate SEM images of the sample surfaces after the immersion in 5 mol/L HCl solution at 25 °C for 10 d. The development of a homogeneous corrosion process for metallic Zr with different grain sizes can be observed. The pitting of the annealed samples shows crystal characters. According to Ref. [42], the surface energy can determine the corrosion rate. Densely arranged planes have lower surface energy with higher binding energy. Atoms on the planes with smaller packing density will potentially undergo rapid corrosion or dissolve more readily, since the activation energy for sample dissolution varies with the magnitude of the packing density^[43]. Fig. 11g shows the sample mass variation with exposure time of pure Zr immersed in 5 mol/L HCl solution at room temperature (25 °C). It can be seen that the pure Zr in HCl solution does not show significant mass loss, although pitting corrosion occurs, which indicates that pure Zr has good corrosion resistance. Fig. 11h shows the number of pitting pits of different samples after immersion for 10 d.

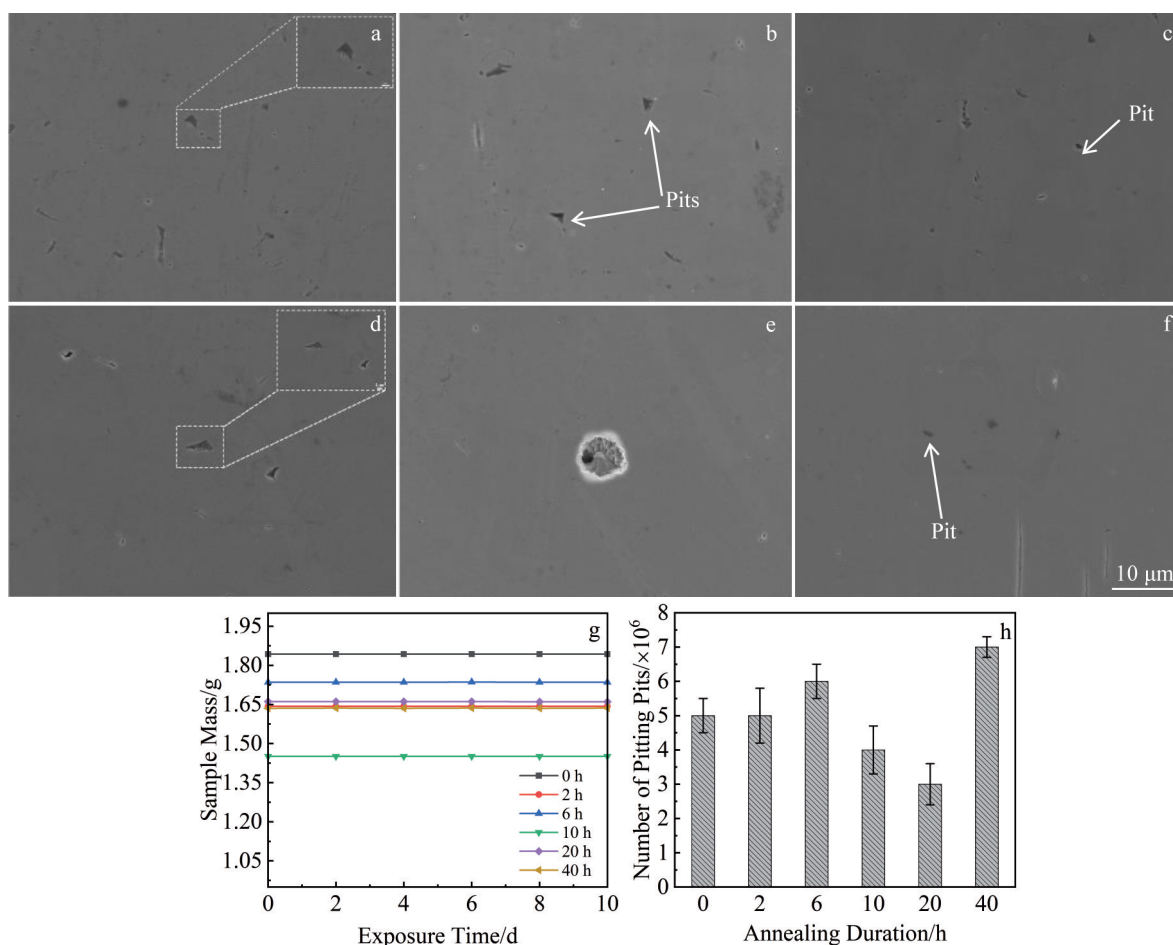


Fig. 11 SEM images of pure Zr after annealing at 800 °C for different durations followed by immersion in 5 mol/L HCl solution at 25 °C for 10 d: (a) 0 h, (b) 2 h, (c) 6 h, (d) 10 h, (e) 20 h, and (f) 40 h; relationship between sample mass and exposure time (g); number of pitting pits in different samples after immersion for 10 d (h)

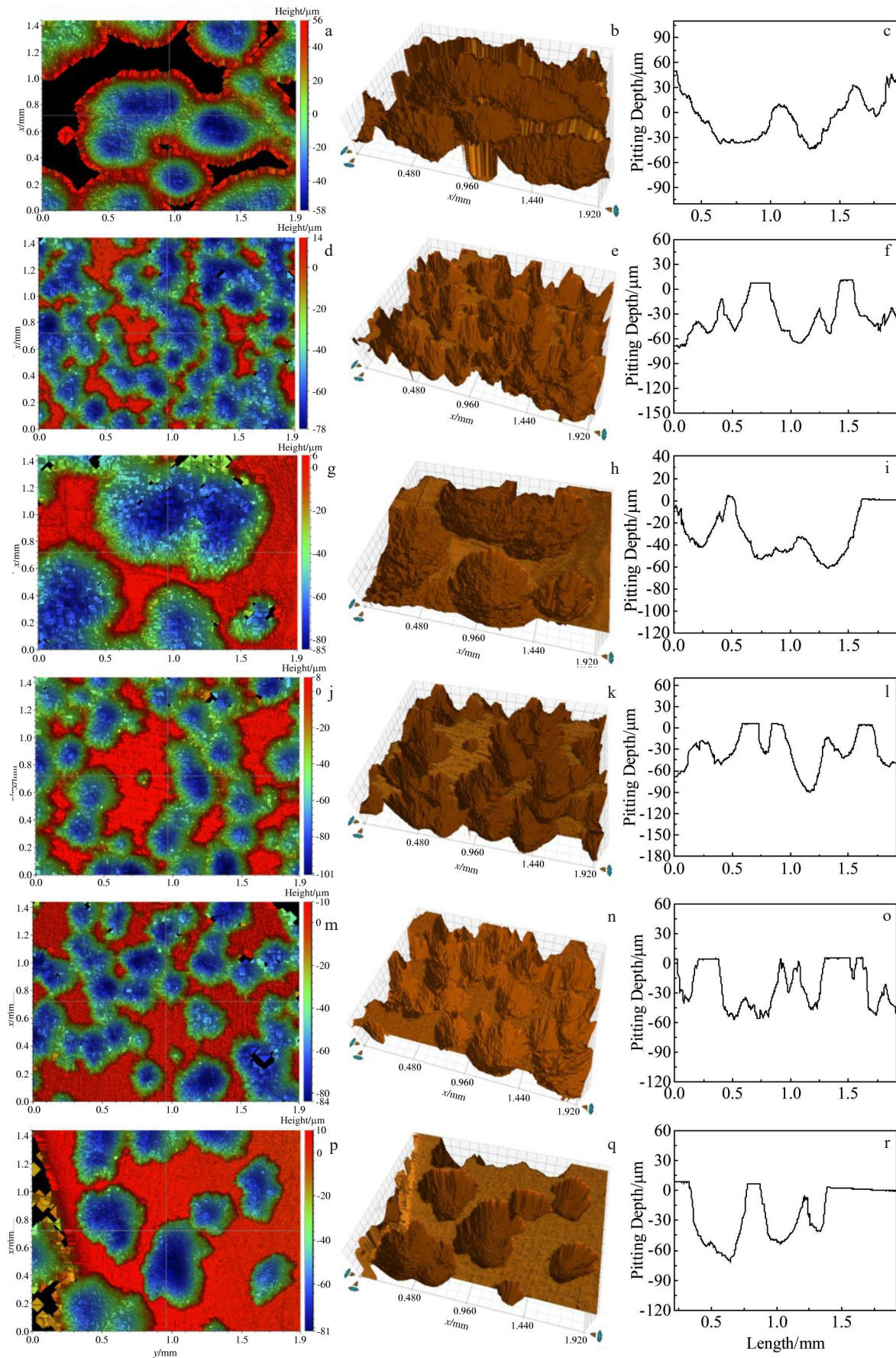
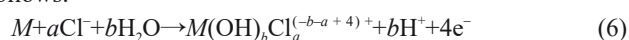


Fig.12 2D morphologies (a, d, g, j, m, p), 3D morphologies (b, e, h, k, n, q), and depth contours (c, f, i, l, o, r) of pitting corrosion of pure Zr after annealing at 800 °C for different durations followed by immersion in 5 mol/L HCl solution at 25 °C for 10 d: (a–c) 0 h, (d–f) 2 h, (g–i) 6 h, (j–l) 10 h, (m–o) 20 h, and (p–r) 40 h

Therefore, with the increase in grain size, the number of pitting pits on the sample surface is firstly increased, then decreased, and finally increased, indicating that the corrosion resistance degrades and improves again. The sample annealed for 20 h has the least number of pitting pits, indicating that its corrosion resistance is optimal. Zr is easily passivated in the air, and its surface is prone to form an oxide film. Pitting process is complex and its mechanisms are still obscure^[44]. Many models^[45] can explain the generation of pitting corrosion, including localized erosion at prior-existing defects in the passivation film, localized acidification, competition between dissolved metals, migration of anions through the passivation film, and competitive adsorption. Besides, the pitting model of passivated aluminum can also be applied to the pitting of passivated Zr^[45]. There is no doubt that the locations of grain boundaries, cracks, defects, and phase boundaries in the oxide film are the primary locations for pitting nucleation. When the aggressive ions (halogen ions) exist in the solution, pitting is much more probable. Therefore, with the presence of chloride ions, pits will be initiated at the abovementioned nucleation sites, and metal dissolution may occur after the pit appearance^[46]. The related formula is as follows:



where a and b are constants; M stands for the metal element.

2.6 Pitting analysis

In order to further analyze the effect of grain size on the corrosion resistance of pure Zr, the corrosion morphology of the sample surface after the polarization test in 5wt% HCl solution was investigated by white light interferometer. 2D and 3D morphologies of the pitting pits on the sample surface are given in Fig. 12, as well as the depth contours of the corrosion pits. The smaller the fluctuation of the pit depth contour, the more intense the surface inhomogeneous corrosion. As shown in Fig. 12, the average depths of the samples after annealing for 0, 2, 6, 10, 20, and 40 h are 64 ± 18.3 , 58 ± 20 , 58.3 ± 8 , 67.8 ± 19.4 , 55.2 ± 6.5 , and 61 ± 14.4 μm , and the depths of pitting pits can be arranged in order as follows: $20 \text{ h} < 2 \text{ h} < 6 \text{ h} < 40 \text{ h} < 0 \text{ h} < 10 \text{ h}$. The larger the pit depth, the more serious the damage to the sample surface. Based on the abovementioned analysis, it is concluded that the pitting pit depth of pure Zr mainly shows an increasing and then decreasing trend with the increase in grain size from 16.51 μm to 23.90 μm . Pure Zr can form passivation film on the surface after open-circuit tests, and the passivation film can resist the destruction of chloride ions and hinder the occurrence of pitting corrosion. In addition, the grain boundaries provide places for the oxide film formation, the film growth is affected, and the protective effect is weakened by the increase in grain size and the decrease in the number of grain boundaries^[47-49].

3 Conclusions

1) The pure Zr after annealing for different durations is composed of equiaxed α -Zr.

2) The grain size of pure Zr ranges from 4 μm to 32 μm . With the increase in grain size, the grain orientation and grain boundary orientation of pure Zr also change. The material exhibits a (0001)/normal direction texture and the sample annealed for 20 h has the highest texture strength.

3) The corrosion resistance of pure Zr is initially decreased, then increased, and subsequently decreased with the increase in grain size. Pure Zr with grain size of approximately 24 μm exhibits the optimal corrosion resistance. The variation in corrosion resistance primarily results in the differences in corrosion current density and immersion pitting.

4) The corrosion behavior of pure Zr is influenced by the combined effects of grain size and texture. Pure Zr with the grain size of approximately 24 μm has the highest degree of orientation strength and forms the thickest oxide film. The enhanced passivation film thickness correlates to the improved corrosion resistance.

References

- Li F, Lin C, Shi Y H et al. *Rare Metal Materials and Engineering*[J], 2022, 51(3): 866
- Wang X Z, Wang Y, Wang Y X et al. *Corrosion Science*[J], 2023, 219: 111226
- Qi B Y, Liu C Z, Yang Q H et al. *Rare Metal Materials and Engineering*[J], 2022, 51(12): 4483
- Yokoyama K, Yamada D, Sakai J. *Corrosion Science*[J], 2013, 73: 375
- Zhang X S, Tong S H, Huang D L et al. *Coordination Chemistry Reviews*[J], 2021, 448: 214177
- Zheng H Q, Zeng Y N, Chen J et al. *Inorganic Chemistry*[J], 2019, 58(10): 6983
- Fattah-Alhosseini A, Chaharmahali R, Keshavarz M K et al. *Surfaces and Interfaces*[J], 2021, 25: 101283
- Mehjabeen A, Song T T, Xu W et al. *Advanced Engineering Materials*[J], 2018, 20(9): 1800207
- Balasubramanian N, Langdon T G. *Metallurgical and Materials Transactions A*[J], 2016, 47: 5827
- Balyanov A J, Kutnyakova N, Amirkhanova A et al. *Scripta Materialia*[J], 2004, 51(3): 225
- Gu Y X, Jiang J H, Ma A B et al. *Journal of Materials Research and Technology*[J], 2021, 15: 1873
- Attarilar S, Djavanroodi F, Irfan O M et al. *Results in Physics*[J], 2020, 17: 103141
- Braga D P, Magalhães D C C, Kliauga A M et al. *Materials Science and Engineering A*[J], 2020, 773: 138865
- Ralston K D, Birbilis N. *Corrosion*[J], 2010, 66(7): 07500
- Nie M Y, Wang C T, Qu M H et al. *Journal of Materials Science*[J], 2014, 49: 2824
- Robson J D. *Journal of Nuclear Materials*[J], 2019, 527: 151814
- Sahoo S K, Panda S, Sabat R K et al. *Philosophical Magazine*[J], 2015, 95(10): 1105
- Ghosh A, Singh A, Gurao N P. *Materials Characteriza-*

- tion[J], 2017, 125: 83
- 19 Kim H S, Kim W J. *Corrosion Science*[J], 2014, 89: 331
- 20 Ding Yumiao, Liu Shuguang, Xia Chaoqun et al. *Surface and Coatings Technology*[J], 2021, 423: 127576
- 21 Sun S, Zai W, Chen Y et al. *Materials Science and Engineering A*[J], 2022, 839: 142802
- 22 Miao Qing, Hu Lianxi, Wang Xin et al. *Journal of Alloys and Compounds*[J], 2010, 493(1-2): 87
- 23 Li Qiang, Chen Kai, Xia Chaoqun et al. *Materials Science and Engineering A*[J], 2021, 817: 141358
- 24 Xu W, Lu X, Wang L N et al. *Journal of the Mechanical Behavior of Biomedical Materials*[J], 2018, 88: 534
- 25 Feng Z H, Dong H C, Kang J et al. *Materials Science and Engineering C*[J], 2019, 101: 92
- 26 Su B X, Luo L S, Wang B B et al. *Journal of Materials Science and Technology*[J], 2021, 62: 234
- 27 Khan M M, Shabib I, Haider W. *Scripta Materialia*[J], 2019, 162: 223
- 28 Kim W G, Choe H C. *Transactions of Nonferrous Metals Society of China*[J], 2009, 19(4): 1005
- 29 Yang Y H, Xia C Q, Feng Z H et al. *Corrosion Science*[J], 2015, 101: 56
- 30 Song T S, Xia C Q, Ding Y M et al. *Corrosion Science*[J], 2022, 208: 110685
- 31 Jiang Z L, Dai X, Norby T et al. *Corrosion Science*[J], 2011, 53(2): 815
- 32 Bolat G, Izquierdo J, Santana J J et al. *Electrochimica Acta*[J], 2013, 88: 447
- 33 Fonseca C, Barbosa M A. *Corrosion Science*[J], 2001, 43(3): 547
- 34 Quintero D, Galvis O, Calderón J A et al. *Surface and Coatings Technology*[J], 2014, 258: 1223
- 35 Eidivandi S, Shayegh B B, Dustmohammadi A et al. *Journal of Alloys and Compounds*[J], 2020, 821: 153253
- 36 Kuczyńska-Zemła D, Sotniczuk A, Pisarek M et al. *Surface and Coatings Technology*[J], 2021, 418: 127219
- 37 Wang Z B, Hu H X, Liu C B et al. *Electrochimica Acta*[J], 2014, 135: 526
- 38 Wang Y H, Li X, Alexandrov I V et al. *Materials*[J], 2020, 13(22): 5117
- 39 Gebert A, Gostin P F, Uhlemann M et al. *Acta Materialia*[J], 2012, 60(5): 2300
- 40 Orłowska M, Ura-Bińczyk E, Adamczyk-Cieślak B et al. *Journal of Materials Science*[J], 2021, 56: 16726
- 41 Sotniczuk A, Chromiński W, Adamczyk-Cieślak B et al. *Corrosion Science*[J], 2022, 200: 110238
- 42 Liu M, Qiu D, Zhao M C et al. *Scripta Materialia*[J], 2008, 58(5): 421
- 43 Xia C Q, Feng Z H, Liu S G et al. *Corrosion Science*[J], 2017, 127: 39
- 44 Soltis J. *Corrosion Science*[J], 2015, 90: 5
- 45 Yasuda M, Weinberg F, Tromans D. *Journal of the Electrochemical Society*[J], 1990, 137(12): 3708
- 46 Hornkjøl S. *Electrochimica Acta*[J], 1988, 33(2): 289
- 47 Gurao N P, Manivasagam G, Govindaraj P et al. *Metallurgical and Materials Transactions A*[J], 2013, 44: 5602
- 48 Lv Xiaodan, Liu Bin, Liu Yan et al. *Materials China*[J], 2022, 41(6): 477 (in Chinese)
- 49 Wu Junyu, Xu Jianping, Liu Houlong et al. *Titanium Industry Progress*[J], 2023, 40(4): 13 (in Chinese)

微观组织结构调控提高纯锆在多种环境下的耐腐蚀性能

夏超群¹, 李可¹, 崔紫尧², 宋天朔¹, 吴鑫雨¹, 刘曙光³, 邹显睿¹, 张士良¹, 杨泰¹, 李强¹

(1. 河北工业大学材料科学与工程学院 天津市材料层状复合与界面控制技术重点实验室, 天津 300401)

(2. 河北工业大学工业技术研究院, 天津 300401)

(3. 北京机械工业自动化研究所有限公司 电气物理设备与应用工程技术中心, 北京 100120)

摘要: 研究了不同晶粒尺寸的纯锆 (Zr) 在酸、碱、盐环境中的腐蚀性能。采用光学显微镜、X射线衍射仪和电子背散射衍射探针对纯 Zr 的微观结构进行观察。采用电化学腐蚀试验和浸泡试验分析纯锆的耐腐蚀性能。结果表明: 800 °C 退火不同时间可获得尺寸为 4~32 μm 的纯 Zr, 晶粒尺寸与时间的关系为 $D^3 - D_0^3 = 3.35t$ 。电化学腐蚀和浸泡腐蚀试验表明, 晶粒尺寸约为 24 μm 的纯 Zr (800 °C 退火 20 h) 具有最佳的耐腐蚀性能。

关键词: 纯锆; 晶粒尺寸; 多种环境; 耐腐蚀性能

作者简介: 夏超群, 男, 1990年生, 博士, 教授, 河北工业大学材料科学与工程学院天津市材料层状复合与界面控制技术重点实验室, 天津 300401, E-mail: chaoqunxia@hebut.edu.cn